

**Transformation pathway and toxic intermediates inhibition of
photocatalytic NO removal on designed Bi metal@defective
 $\text{Bi}_2\text{O}_2\text{SiO}_3$**

**Xinwei Li ^a, Wendong Zhang ^b, Jiyeuan Li ^{a,c}, Guangming Jiang ^a, Ying Zhou ^d,
ShunCheng Lee ^e, Fan Dong ^{a,d*}**

^aChongqing Key Laboratory of Catalysis and New Environmental Materials, College of Environment and Resources, Chongqing Technology and Business University, Chongqing 400067, China.

^b Chongqing Key Laboratory of Inorganic Functional Materials, Department of Scientific Research Management, Chongqing Normal University, Chongqing, 401331, China.

^c College of Architecture and Environment, Institute of New Energy and Low Carbon Technology, Sichuan University, Sichuan 610065, China.

^dThe Center of New Energy Materials and Technology, School of Materials Science and Engineering, Southwest Petroleum University, Chengdu 610500, China.

^e Department of Civil and Environmental Engineering, The Hong Kong Polytechnic University, Hong Kong, China.

*Corresponding author. E-mail: dfctbu@126.com, tel.: +86 23 62769785 605, fax: +86 23 62769785 605.

Abstract: The design of highly efficient visible-light photocatalysts and the elucidation of decomposition mechanisms are the two key tasks in environmental remediation. Herein, we utilized theoretical calculations to design a Bi metal-based visible-light photocatalyst (Bi@BiOSi) with surface plasmon resonance (SPR) properties, showing that the unique electron delivery channel was formed at the Bi metal/Bi₂O₂SiO₃ interface. The Bi@BiOSi nanosheets were used for photocatalytic removal of ppb-level atmospheric NO, with Bi metal-based SPR resulting in enhanced visible light capture and charge separation efficiency, whereas oxygen vacancy induced the formation of a midgap level and promoted O₂ activation. As a result, generation of superoxide and hydroxyl radicals over Bi@BiOSi was promoted, favoring photocatalytic NO removal. To elucidate the reaction mechanism, the products distribution during adsorption and photocatalytic NO oxidation on Bi@BiOSi were determined by in situ DRIFTS, which revealed that the increased production of reactive species inhibited the toxic intermediates (N₂O₄) formation and increased the selectivity of the NO-to-NO₃⁻ transformation via the synergy of oxygen vacancy and Bi metal. Thus, this work provides new insights into the design of non-noble metal-based photocatalysts and establishes a novel method of inhibiting the toxic intermediates production in photocatalysis for efficient and safe air purification.

Keywords: Bi metal; Oxygen vacancy; photocatalysis; toxic intermediates inhibition; in situ DRIFTS.

1. Introduction

NO is one of the major air pollutants emitted by vehicles and power plants [1-3], being a typical PM_{2.5} precursor and playing an important role in the formation of haze and photochemical smog [4,5]. Generally, chemical removal of NO is mainly achieved using conventional approaches such as selective catalytic reduction [6], three-way catalysis [7], wet scrubbing [8], biofiltration [9], and oxidation-adsorption processes [10]. However, all these processes are generally developed for the removal of high-concentration NO from industrial emissions, being not economically suitable for use in urban atmospheric environments, which are characterized by NO concentration of parts per billion (ppb). However, photocatalysis is regarded as an alternative low-concentration NO removal technology due to its energy saving potential, low cost, and green easy-to-operate character [11-14].

In general, the reactive radical-mediated photocatalytic oxidation of NO affords nitrate ions adsorbed on the catalyst surface, which are easily washed away [15,16]. However, in certain cases, photocatalytic oxidation is undesirable due to its potential of concomitantly producing toxic intermediates such as NO₂ and N₂O₄ that are released into the atmosphere and subsequently cause secondary pollution [17-19]. Thus, despite being largely ignored, the above issue presents a major challenge for the application of photocatalysis in air purification.

Although noble metal (Pt, Pd, Au)-based co-catalysts have been reported to inhibit the formation of toxic intermediates during photocatalytic oxidation of aqueous contaminants [20-22], their widespread application is hindered by high cost.

Moreover, the complicated mechanism of photocatalytic NO oxidation in air remains incompletely understood. Recently, Dong et al. found that Bi, a non-noble metal, demonstrates direct plasmonic photocatalytic performance [23], which allows it to be used as a noble metal substitute to improve the photocatalytic performance of other semiconductors [24-27]. Thus, the fabrication of a Bi metal-based model photocatalyst should contribute to our detailed understanding of the NO removal mechanism, particularly to that of toxic intermediate generation, an important issue that has been largely overlooked. This could help to establish effective approaches of inhibiting the formation of such intermediates during photocatalytic NO oxidation.

Herein, we designed and fabricated Bi metal@Bi₂O₂SiO₃ (Bi@BiOSi) as a model catalyst, utilizing density functional theory (DFT) calculations to predict the optimized electronic structure of Bi@BiOSi and the mechanism of charge transfer between its constituents. Based on DFT insights, Bi@BiOSi composites were fabricated via a facile chemical reduction method and used for the removal of ppb-level NO in a continuous air flow reactor under visible light illumination, with the obtained results demonstrating the simultaneous deposition of Bi metal and formation of oxygen vacancies (OVs). Moreover, Bi metal with SPR effect and working as electron sink enhanced the visible light capture and charge separation efficiencies, whereas OV generation induced the formation of a midgap level to make Bi@BiOSi catalysts visible light active. At the same time, the coexistence of OVs and Bi metal had synergistic effects on NO and O₂ activation on catalyst. Consequently, the production of both superoxide and hydroxyl radicals on Bi@BiOSi was

significantly enhanced, leading to much more efficient photocatalytic NO removal under visible light irradiation. Most importantly, the adsorption and photocatalytic oxidation of NO on Bi@BiOSi were investigated by in situ DRIFTS, which revealed that the enhanced production of reactive species inhibited the generation of toxic intermediates (N_2O_4) and increased the selectivity of the NO-to- NO_3^- conversion.

2. Experimental

Details of catalyst preparation, Characterization method and theoretical calculation methods are given in Supporting Information.

2.1 Evaluation of Visible Light Photocatalytic Activity. The photocatalytic activities of as-prepared samples were evaluated by removal of ppb-level NO in a continuous flow reactor under visible light irradiation, with detailed procedures presented in the Supporting Information (**Fig. S1**).

2.2 In situ DRIFTS investigation of the photocatalytic NO oxidation mechanism. In situ DRIFTS measurements (**Fig. S3**) were conducted using a TENSOR II Fourier transform infrared (FT-IR) spectrometer (Bruker) equipped with an in situ diffuse reflectance cell (Harrick) and a high-temperature reaction chamber (HVC), which featured two gas ports and two cooling ports. High-purity He, high-purity O_2 , and 100 ppm NO in He were fed into the reaction system, and a three-way ball valve was used for switching between target (NO) and purge (He) gases. The total gas flow rate equaled 100 mL/min, and the concentration of NO was controlled at 50 ppm by dilution with O_2 . The chamber was enclosed within a dome with three windows: two IR light-transparent ZnSe windows and one UV

light-transparent quartz window for photocatalyst illumination. A Xe lamp (MVL-210, Optpe, Japan) (**Fig. S3e**) was used as the light source.

3. Results and discussion

3.1 Theoretical design of the Bi@BiOSi model catalyst. The BiOSi catalyst comprised $[\text{Bi}_2\text{O}_2]^{2+}$ slabs sandwiched between SiO_3^{2-} pyroxene file layers [28,29]. In the first step, we modeled and optimized the electronic configuration of Bi@BiOSi, which typically featured exposed (311) facets with one Bi particle layer homogenously deposited on the above facet (**Fig. S4**) [30]. The effect of top Bi metal could be well understood by employing the projected density of states (**Fig. 1a**). Notably, the positive shift of the Bi β peak of Bi@BiOSi relative to that of pristine BiOSi indicated that Bi atoms in Bi@BiOSi possessed a higher electron distribution. The corresponding partial decomposed charge densities further confirmed that it is the top Bi layer carrying more charge (**Fig. S5**). Then, the electron localization functional shown in **Fig. S6** illustrates the existence of a covalent interaction between top Bi layer and substrate BiOSi (311), whereas the charge difference distribution (**Fig. 1b**) reveals that random electrons would migrate from BiOSi to the top Bi layer causing charge accumulation over top Bi atoms. The number of top Bi atoms did not affect the charge transfer direction (**Fig. S7**). Further, the electrostatic potential of Bi@BiOSi configuration presented in **Fig. S8** implies that Bi metal lower the electron transfer energy due to working as an electron sink to ensure the directional movement of electrons from BiOSi to top Bi metal. Hence, the Bi@BiOSi configuration would

originally improve the charge transport at the interface by Bi metal incessantly attracting charge transfer.

Fig.1

3.2 Synthesis and structure of Bi@BiOSi. Since the deposition of Bi metal on BiOSi could promote the separation and transfer of charges as key photocatalysis steps, we used NaBH₄ as a reducing agent to achieve Bi metal deposition on the surface of BiOSi. The X-ray diffraction (XRD) patterns of as-prepared samples (**Fig. 2a**) showed that the diffraction peaks of BiOSi were well matched with the orthorhombic phase of Bi₂O₂SiO₃ (PDF#75-1483) [31], with their intensity decreasing with increasing NaBH₄ concentration. Moreover, a new phase, namely rhombohedral Bi metal (PDF#85-1330) was observed in Bi@BiOSi-3 and Bi@BiOSi-4, with its peak becoming dominant in Bi@BiOSi-5 and thus implying the complete reduction of Bi³⁺ in BiOSi to Bi metal. Similar to XRD analysis, all FT-IR spectra (**Fig. S9**) relevant characteristic peaks were disordered in the spectra of Bi@BiOSi-4, being totally absent in those of Bi@BiOSi-5.

Fig. 2b shows the XPS spectra of Bi4f, where the two peaks located at 164.2 and 158.8 eV for BiOSi sample are attributed to Bi4f_{7/2} and Bi4f_{5/2} peaks of Bi³⁺ respectively [12, 32]. In contrast, there are two additional peaks at 161.8 and 156.7 eV assigned to Bi⁰ in Bi@BiOSi-3 [33]. Moreover, Bi 4f (**Fig. 2b**) and O 1s (**Fig. S10c**) peaks of Bi@BiOSi-3 had higher binding energies than those of pristine BiOSi, suggesting the existence of a covalent interaction between Bi metal and BiOSi, in agreement with theoretical calculations [34,35]. The atomic content of Bi³⁺, Bi⁰, Si

and O elements and the ratio of Bi metal to $\text{Bi}_2\text{O}_2\text{SiO}_3$ of the samples are given in Table S1. Considering that Bi metal is in situ introduced on the surface of BiOSi, the interfacial contact between BiOSi and Bi is intimate, promoting interfacial charge transfer.

Scanning electron microscopy (SEM) and transmission electron microscopy (TEM) were employed for morphological characterization, revealing that pure BiOSi comprised interconnected ultrathin nanosheets (**Fig. 2c**, S11a, b and S12a, b). Correspondingly, small nanoparticles uniformly distributed on nanosheets were observed for Bi@BiOSi-3 (**Fig. 2d**, S11c, d and S12c, d). Representative high-resolution TEM (HRTEM) images of BiOSi and Bi@BiOSi-3 (**Fig. S13a, b and c, d**, respectively) revealed that in situ formed Bi nanoparticles with mean particle size of 4.0 nm (**Fig. S14**) were dispersed on the surface of BiOSi nanosheets. The BET surface area of Bi@BiOSi samples are 27.2, 29.0, 29.8, 26.3, 28.8 m^2/g , respectively, all higher than that of bulk BiOSi (19.7 m^2/g). With more nanoparticle metal Bi deposited on the surface, the BET surface areas are increased. N_2 adsorption-desorption isotherm and pore diameter distributions of samples are given in **Fig. S15**. Moreover, the lattice spacing of 0.328 nm (**Fig. 2e**) identified in the nanoparticle region (circled part) was well matched with the (012) plane of rhombohedral Bi.

Fig. 2

3.3 Visible light photocatalytic NO removal. The as-prepared catalysts were used for photocatalytic NO removal under visible light illumination in a continuous air

flow reactor, with the obtained results (**Fig. 3a**) showing that pristine BiOSi exhibited negligible visible light activity. However, Bi metal deposition significantly improved the photocatalytic activity, with the highest NO removal efficiency of 50.2% observed for Bi@BiOSi-3 being followed by those of Bi@BiOSi-2 (38.6%), Bi@BiOSi-4 (27.7%), Bi@BiOSi-1 (14.2%), and Bi@BiOSi-5 (13.8%). The corresponding NO₂ generations are given in **Fig. S16**. Nevertheless, the excessive amounts of Bi metal in Bi@BiOSi-4 and Bi@BiOSi-5 were expected to negatively affect photocatalytic activity. Notably, Bi@BiOSi-3 exhibits superior photocatalytic activity in comparison with common photocatalysts P25 and g-C₃N₄ (**Fig. S17**).

After the photocatalytic activity test, the final products NO₂⁻ and NO₃⁻ on the catalysts surface were washed with 100 mL deionized water and determined by ion chromatography (IC) (**Fig. S18**). The NO₂⁻ and NO₃⁻ are the final products of photocatalytic NO oxidation. The concentration of NO₂⁻ and NO₃⁻ accumulated on different catalyst is consistent with the photocatalytic activity, i.e. the most efficient Bi@BiOSi-3 generated maximum amount of NO₃⁻ product on the catalyst surface. The durability of Bi@BiOSi-3 was further tested for five repeated irradiations (**Fig. S19a**), which implies that the Bi@BiOSi was photo-chemically stable with little deactivation. Catalyst XRD and XPS comparison after repeated experiments are also give in Fig. S19b-d

3.4 Optical properties and band structure. Since Bi metal exhibits visible light-induced surface plasmon resonance (SPR) effect [36], Bi@BiOSi samples showed enhanced visible light capture ability (**Fig. 3b**). In these samples, Bi metal

could concentrate incident photon energy into plasmon oscillations and thus significantly enhanced the electromagnetic field (simulated by FDTD techniques in **Fig. S20**) to facilitate the separation of electrons (e^-) and holes (h^+) [37-39]. The characteristic PL peaks of Bi@BiOSi (**Fig. S21**) were significantly less intense than those of BiOSi, further implying that the introduction of Bi metal inhibited charge carrier recombination.

Fig. 3

Plots of $(ah\nu)^{1/2}$ versus photon energy and the valence-band XPS spectra of BiOSi and Bi@BiOSi-3 (**Fig. S22**) showed that Bi metal introduction did not significantly affect the band gap energy and the valence band position [40,41]. Since the conduction band edge of Bi@BiOSi-3 (-1.03 eV) was more negative than that of the Fermi level of Bi metal (-0.17 eV) [23], the BiOSi-to-Bi flow of photoexcited electrons in Bi@BiOSi-3 was thermodynamically favorable. However, the band gap of BiOSi is 3.2 eV (**Fig. S22a**), which can be hardly excited under visible light irradiation.

The solid-state electron paramagnetic resonance (EPR) is employed to investigate the nature of defects under room temperature [42]. There are little OVs in BiOSi as the EPR signal in dark is negligible (**Fig. 4a**). However, the Bi@BiOSi samples show gradually enhanced EPR signal with the increase amount of Bi metal at $g = 2.004$, implying that an increased amount of OVs was generated [41]. Also, these EPR signals are found to be intensified under visible light irradiation, further confirming that the charge mobility of Bi@BiOSi samples can be effectively promoted for Bi

metal [43-45]. More importantly, OV's would induce the formation of an intermediate level, as revealed by DFT calculations (**Fig. S23**), allowing photo-electron excited from the valence band to the intermediate level and then to the conduction band to induce following reactions (**Fig. S24**) [46].

3.5 Reactants activation. The adsorption of O₂ and NO on the catalyst surface is a key step in gas-solid photocatalytic reaction. Firstly, O₂ activation is a quite essential step by producing active free radicals that directly work on contaminates. Also, O₂ activation could trap electrons thus effectively prevent carrier recombination. Therefore, the most stable O₂ adsorption results (**Fig. S25**) after optimizing the initial configurations are obtained to get access to the effect of OV's and Bi metal for O₂ activation. Apparently, O-O bond length is enlarged on both OV-BiOSi and Bi-BiOSi configurations. Moreover, the energy of O₂ molecule adsorption (E_{ads}) in the four structures are: OV-BiOSi (-2.29 eV) < side-Bi-BiOSi (-1.84 eV) < BiOSi (-1.61 eV) < top-Bi-BiOSi (-1.41 eV). These results suggest that side-Bi-BiOSi configuration would facilitate O₂ activation to certain extent while OV-BiOSi is the most beneficial configuration for O₂ adsorption and activation for its most negative E_{ads} and largely lengthened O-O bond. Normally, surface OV's could supply coordinately unsaturated sites for O₂ adsorption and activation and thus promote superoxide radical ($\bullet\text{O}_2^-$) formation [47]. Consequently, enhanced ESR signals of DMPO- $\bullet\text{O}_2^-$ (**Fig. 4b**) could be observed for Bi@BiOSi-3 compared with pristine BiOSi. Additionally, the enhanced ESR signals of hydroxyl radicals ($\bullet\text{OH}$) (**Fig. S26**) can be ascribed to increased charge separation efficiency.^{12, 29} The observed $\bullet\text{OH}$ were formed via the

oxidation of surface OH^- by photogenerated h^+ , since the potential energy of valence-band h^+ (2.05 eV) was higher than that of $\text{OH}^-/\bullet\text{OH}$ (1.99 eV) [12,48]. Thus, the increased production of highly oxidizing active radicals favored the complete oxidation of NO.

In addition, NO adsorption over the four configurations was calculated as shown in **Fig. S27**. The side-Bi-BiOSi is the most favorable configuration for NO adsorption as indicated by the most negative adsorption energy and largely lengthened N-O bond. According to the total charge calculated by Bader method [49], Bi metal could facilitate the NO by accepting electrons, while the OVs promote NO activation by donating electrons.

In the actual reaction situation, the O_2 and NO coexist on the catalyst surface. Therefore, we discussed the NO and O_2 co-adsorption on OV-BiOSi and side-Bi-BiOSi structure that either in favors of O_2 adsorption or NO adsorption. In the presence of OVs (**Fig. 4c**), O_2 is preferentially adsorbed and activated for its largely lengthened O-O bond. While the adsorption of NO seems to be limited when coexisting with O_2 for its shorten N-O bond. Also the density difference result shows that the random electrons are accumulated on O_2 for its activation in priority.

For side-Bi-BiOSi structure (**Fig. 4d**), it could be seen that the NO is prior to receive electrons from Bi metal then transfer them to O_2 for its activation. Also, Bi metal would not prevent O_2 from adsorption while promoting NO adsorption in side-Bi-BiOSi structure according to N-O and O-O bond length variation. Interestingly, the total charge of NO in the two structures remains unchanged,

including the electron loss in OV-BiOSi and charge accumulation in side-Bi-BiOSi. The as-prepared catalyst is largely influenced by OVs and Bi metal. That is to say, it is favorable for O₂ activation on OVs dominated area, whereas the NO adsorption would be promoted by Bi metal.

Fig. 4

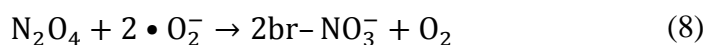
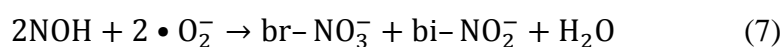
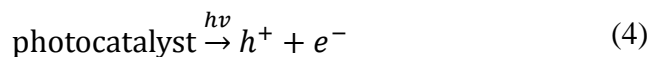
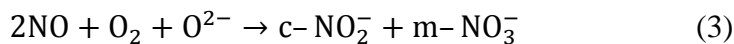
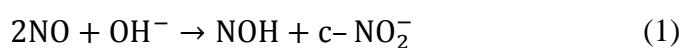
3.6 Mechanism of photocatalytic NO oxidation and toxic intermediates inhibition. The mechanism of photocatalytic NO oxidation was probed by in situ DRIFTS to directly monitor NO and O₂ adsorption and reactions on the catalyst surface. In situ DRIFT spectra recorded during adsorption and photocatalytic reaction on BiOSi and Bi@BiOSi samples as shown in **Fig. S28** and **Fig. 5**. NO and O₂ led to the formation of several adsorbed NO_x species with adsorption bands attribution shown in Table S3.

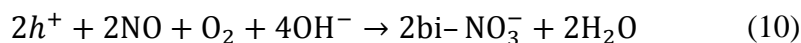
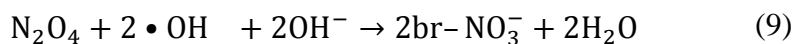
During adsorption (**Fig. S28**), NO (1715-1724 cm⁻¹) is capable of simultaneously reacting with surface hydroxyl groups (broad 3300 cm⁻¹) to form NOH (around 1100 cm⁻¹) and bi-NO₂⁻ (1590, 1594 cm⁻¹) (Eq. 1) with quite low content [50, 51-53]. Also, NO together with O₂ is more like to convert into N₂O₄ (1376-1350 cm⁻¹) [54], the dipolymer of NO₂, that is an undesirable toxic intermediates (Eq. 2). However, NO may react with neighboring O₂ present at the OVs (O₂²⁻) to afford surface-adsorbed c-NO₂⁻ and m-NO₃⁻ (Eq. 3) to prevent N₂O₄ generation [48]. That is to say, gradual generated OVs in Bi@BiOSi samples are able to inhibit the conversion of NO into N₂O₄ during the adsorption period to extent.

After photocatalytic reaction sparked, •O₂⁻ and •OH radicals would be produced

via photoexcited h^+ and e^- reacted with surface O_2 and OH^- , respectively (Eqs. 4-6), being subsequently utilized for the oxidation of NOH and N_2O_4 to bi- NO_2^- and br- NO_3^- (1695 cm^{-1}) thoroughly (Eqs. 7-9) [53]. That is to say, sufficient generated active radicals are able to oxidize all intermediates completely avoiding toxic intermediates accumulation effectively. Moreover, photoexcited h^+ could also directly oxidize NO to bi- NO_3^- (1404 cm^{-1}) (Eq. 10) [52,55]. The overall process of NO adsorption and photocatalytic oxidation in Bi@BiOSi sample is given in **Fig. S29**. Control experiments on DRIFT spectra over P25, CN and without photocatalyst are given in **Fig. S30**. There is no detectable IR peak under both dark and light on situation, without photocatalyst which means NO would not be removed without photocatalytic reaction. On the other hand, NO^+ , NO, N_2O_4 , NO_2^- and NO_3^- are detected over CN and P25 under light irradiation, which are common photocatalytic NO oxidation intermediates and final products [56-58].

Fig. 5





The normalization method was used to Figure out the intermediates difference during adsorption and reaction stage (**Fig. 6**). The content percentage means the one single species as a percentage of total NO_x intermediates species of each sample after adsorption and reaction stage.

Form the product percentage shown in **Fig. 6a**, the main product on BiOSi during dark adsorption is N₂O₄. Also, the yield of N₂O₄ is highest in BiOSi among all samples in adsorption stage. However, the generation of N₂O₄ in this stage is decreased from Bi@BiOSi-1 to Bi@BiOSi-4 sample with gradual increased OVs and Bi metal, which means the generation of N₂O₄ is suppressed in the adsorption phase. As for Bi@BiOSi-5 samples, no characteristic peaks can be detected.

For the photocatalytic reaction stage, certain content of NO⁺ and NO₂⁺ can be detected in Bi@BiOSi-1 and Bi@BiOSi-2 samples as shown in **Fig. 6b** [49]. That is to say, the NO and NO₂ tend to lose electrons in Bi@BiOSi-1 and Bi@BiOSi-2 samples. In combination with DFT, the OVs play a main role in these two samples as NO is more like to be electron donor. Nevertheless, NO⁺ and NO₂⁺ are not detected in Bi@BiOSi-3 and Bi@BiOSi-4 with increased amount of Bi metal which is prone to donate electrons to the adsorbed NO. It is worth noting that the generation of final products NO₂⁻ and NO₃⁻ reaches to the highest level in Bi@BiOSi-3 samples during photocatalysis reaction, which is accounted for its most positive response in NO removal. The selectivity of the NO-to-NO₃⁻ transformation during photocatalysis

could be improved largely with combined effect of OVs and Bi metal. There is still no any peak being detected in Bi@BiOSi-5 samples after light on, which indicates that the excessive Bi metal is wrapped on the surface of the catalyst, which would prevent NO from adsorption on the catalyst surface (**Fig. S27**).

Fig. 6

In general, the photocatalytic NO removal would reach maximum when the content of OVs and Bi metal is optimized. The “volcano-like” variation of the photocatalytic activity of Bi@BiOSi samples should be ascribed to the synergy of OVs and Bi metal, which can be schemed in **Fig. 7**.

Fig. 7

Thus, Bi@BiOSi is an outstanding photocatalyst for efficient and safe air purification. The detailed photocatalytic reaction mechanism is illustrated in **Fig. 8**.

Fig. 8

4. Conclusion

Although only a model Bi@BiOSi catalyst is described herein, this study has significant implications for modification of the abundant Bi-containing semiconductors. Bi metal was shown to increase the visible light absorption and carrier transportation efficiency of the studied photocatalyst due to exhibiting SPR properties and working as electron sink. Meanwhile, the simultaneously generated OVs form an intermediate energy level, making it possible for the wide band gap semiconductor being responded to visible light. Moreover, the co-existed OVs and Bi

metal were demonstrated to have synergy effect on reactants activation on the catalyst surface. These parameters are decisive factors for sufficient active radical generation during photocatalysis. Then, the generation of N_2O_4 was effectively inhibited during adsorption as well as reaction process by the largely produced active radicals via in situ DRIFTS monitoring. Finally, the high selectivity of the NO -to- NO_3^- transformation is accomplished by the synergy of OVs and Bi metal. The above insights should enable the modification of other Bi-containing semiconductors to highly inhibit the generation of toxic intermediates, an important issue that has been largely overlooked.

Acknowledgements

This work was supported by the National Natural Science Foundation of China (21822601, 21777011, and 21501016), the National R&D Program of China (2016YFC0204702), the Innovative Research Team of Chongqing (CXTDG201602014), the Natural Science Foundation of Chongqing (cstc2017jcyjBX0052), and the Plan for "National Youth Talents" of the Organization Department of the Central Committee. The authors also acknowledge AM-HPC in Suzhou, China for computational support.

Reference

[1] M. Jacobson, W. Colella, D. Golden, Cleaning the air and improving health with hydrogen fuel-cell vehicles, *Science*, 308 (2005) 1901-1905.

- [2] J.J. Schauer, M.J. Kleeman, G.R. Cass, B.R.T. Simoneit, Measurement of Emissions from Air Pollution Sources. 5. C₁–C₃₂ Organic Compounds from Gasoline-Powered Motor Vehicles, *Environmental Science & Technology*, 36 (2002) 1169-1180.
- [3] H. Wang, W. He, X. Dong, H. Wang, F. Dong, In Situ FT-IR Investigation on the Reaction Mechanism of Visible Light Photocatalytic NO Oxidation with defective g-C₃N₄, *Science Bulletin*, 63 (2018) 117-125.
- [4] X. Querol, A. Alastuey, S. Rodriguez, F. Plana, C.R. Ruiz, N. Cots, G. Massagué, O. Puig, PM₁₀ and PM_{2.5} source apportionment in the Barcelona Metropolitan area, Catalonia, Spain, *Atmospheric Environment*, 35 (2001) 6407-6419.
- [5] X. Wang, J. Chen, T. Cheng, R. Zhang, X. Wang, Particle number concentration, size distribution and chemical composition during haze and photochemical smog episodes in Shanghai, *Journal of Environmental Sciences*, 26 (2014) 1894-1902.
- [6] M. Casapu, O. Kröcher, M. Elsener, Screening of doped MnO_x–CeO₂ catalysts for low-temperature NO-SCR, *Applied Catalysis B: Environmental*, 88 (2009) 413-419.
- [7] T. Kobayashi, T. Yamada, K. Kayano, Effect of basic metal additives on NO_x reduction property of Pd-based three-way catalyst, *Applied Catalysis B: Environmental*, 30 (2001) 287-292.
- [8] J. Wei, Y. Luo, P. Yu, B. Cai, H. Tan, Removal of NO from flue gas by wet scrubbing with NaClO₂/(NH₂)₂CO solutions, *Journal of Industrial and Engineering Chemistry*, 15 (2009) 16-22.
- [9] S.P.P. Ottengraf, Biological systems for waste gas elimination, *Trends in*

Biotechnology, 5 (1987) 132-136.

[10] A. Ishihara, D. Wang, F. Dumeignil, H. Amano, E.W. Qian, T. Kabe, Oxidative desulfurization and denitrogenation of a light gas oil using an oxidation/adsorption continuous flow process, *Applied Catalysis A: General*, 279 (2005) 279-287.

[11] H. Wang, Y. Sun, G. Jiang, Y. Zhang, H. Huang, Z. Wu, S. C. Lee, F. Dong, Unraveling the Mechanisms of Visible Light Photocatalytic NO Purification on Earth-Abundant Insulator-Based Core-Shell Heterojunctions, *Environmental Science & Technology*, 52 (2018), 1479-1487.

[12] Z. Ai, W. Ho, S. Lee, L. Zhang, Efficient Photocatalytic Removal of NO in Indoor Air with Hierarchical Bismuth Oxybromide Nanoplate Microspheres under Visible Light, *Environmental Science & Technology*, 43 (2009) 4143-4150.

[13] Y. Lu, Y. Huang, Y. Zhang, J.-j. Cao, H. Li, C. Bian, S.C. Lee, Oxygen vacancy engineering of $\text{Bi}_2\text{O}_3/\text{Bi}_2\text{O}_2\text{CO}_3$ heterojunctions: Implications of the interfacial charge transfer, NO adsorption and removal, *Applied Catalysis B: Environmental*, 231 (2018) 357-367.

[14] Q. Zhang, Y. Huang, S. Peng, Y. Zhang, Z. Shen, J. J. Cao, W. Ho, S.C. Lee, D.Y. Pui, Perovskite $\text{LaFeO}_3\text{-SrTiO}_3$ composite for synergistically enhanced NO removal under visible light excitation, *Applied Catalysis B: Environmental*, 204 (2017) 346-357.

[15] F. Dong, Z. Wang, Y. Li, W.-K. Ho, S.C. Lee, Immobilization of Polymeric $\text{g-C}_3\text{N}_4$ on Structured Ceramic Foam for Efficient Visible Light Photocatalytic Air Purification with Real Indoor Illumination, *Environmental Science & Technology*, 48 (2014)

10345-10353.

[16] W. Cui, J. Li, Y. Sun, H. Wang, G. Jiang, S.C. Lee, F. Dong, Enhancing ROS generation and suppressing toxic intermediate production in photocatalytic NO oxidation on O/Ba co-functionalized amorphous carbon nitride, *Applied Catalysis B: Environmental*, 237 (2018) 938-946.

[17] Y. Byun, K.B. Ko, M. Cho, W. Namkung, K. Lee, D. N. Shin, D.J. Koh, Reaction Pathways of NO Oxidation by Sodium Chlorite Powder, *Environmental Science & Technology*, 43 (2009) 5054-5059.

[18] P.E. Morrow, Toxicological data on NO_x : An overview, *Journal of Toxicology and Environmental Health*, 13 (1984) 205-227.

[19] A.M. Winer, G.M. Breuer, W.P.L. Carter, K.R. Darnall, J.N. Pitts, Effects of ultraviolet spectral distribution on the photochemistry of simulated polluted atmospheres, *Atmospheric Environment* (1967), 13 (1979) 989-998.

[20] Z. Zheng, B. Huang, X. Qin, X. Zhang, Y. Dai, M.-H. Whangbo, Facile in situ synthesis of visible-light plasmonic photocatalysts M@TiO₂ (M = Au, Pt, Ag) and evaluation of their photocatalytic oxidation of benzene to phenol, *Journal of Materials Chemistry*, 21 (2011) 9079-9087.

[21] P. Roy, A.P. Periasamy, C.-T. Liang, H. T. Chang, Synthesis of Graphene-ZnO-Au Nanocomposites for Efficient Photocatalytic Reduction of Nitrobenzene, *Environmental Science & Technology*, 47 (2013) 6688-6695.

[22] T. Sano, S. Kutsuna, N. Negishi, K. Takeuchi, Effect of Pd-photodeposition over TiO₂ on product selectivity in photocatalytic degradation of vinyl chloride monomer,

Journal of Molecular Catalysis A: Chemical, 189 (2002) 263-270.

[23] F. Dong, T. Xiong, Y. Sun, Z. Zhao, Y. Zhou, X. Feng, Z. Wu, A semimetal bismuth element as a direct plasmonic photocatalyst, *Chemical Communications*, 50 (2014) 10386-10389.

[24] J. Gong, A. Imbault, R. Farnood, The promoting role of bismuth for the enhanced photocatalytic oxidation of lignin on Pt-TiO₂ under solar light illumination, *Applied Catalysis B: Environmental*, 204 (2017) 296-303.

[25] M. Chen, Y. Li, Z. Wang, Y. Gao, Y. Huang, J. Cao, W. Ho, S. Lee, Controllable Synthesis of Core-Shell Bi@Amorphous Bi₂O₃ Nanospheres with Tunable Optical and Photocatalytic Activity for NO Removal, *Industrial & Engineering Chemistry Research*, 56 (2017) 10251-10258.

[26] L. Yan, Z. Gu, X. Zheng, C. Zhang, X. Li, L. Zhao, Y. Zhao, Elemental Bismuth-Graphene Heterostructures for Photocatalysis from Ultraviolet to Infrared Light, *ACS Catalysis*, 7 (2017) 7043-7050.

[27] R.A. Patil, M.-K. Wei, P.H. Yeh, J.-B. Liang, W. T. Gao, J.-H. Lin, Y. Liou, Y.-R. Ma, Size-controllable synthesis of Bi/Bi₂O₃ heterojunction nanoparticles using pulsed Nd: YAG laser deposition and metal-semiconductor-heterojunction-assisted photoluminescence, *Nanoscale*, 8 (2016) 3565-3571.

[28] S. Georges, F. Goutenoire, P. Lacorre, Crystal structure of lanthanum bismuth silicate Bi_{2-x}LaxSiO₅ (x~0.1), *Journal of Solid State Chemistry*, 179 (2006) 4020-4028.

[29] D. Liu, J. Wang, M. Zhang, Y. Liu, Y. Zhu, A superior photocatalytic performance

of a novel Bi_2SiO_5 flower-like microsphere via a phase junction, *Nanoscale*, 6 (2014) 15222-15227.

[30] A.K.R. Police, S. Basavaraju, D.K. Valluri, S. Machiraju, Bismuth Modified Porous Silica Preparation, Characterization and Photocatalytic Activity Evaluation for Degradation of Isoproturon, *Journal of Materials Science & Technology*, 29 (2013) 639-646.

[31] J. Di, J. Xia, Y. Huang, M. Ji, W. Fan, Z. Chen, H. Li, Constructing carbon quantum dots/ Bi_2SiO_5 ultrathin nanosheets with enhanced photocatalytic activity and mechanism investigation, *Chemical Engineering Journal*, 302 (2016) 334-343.

[32] X. Ding, W. Ho, J. Shang, L. Zhang, Self doping promoted photocatalytic removal of no under visible light with Bi_2MoO_6 : Indispensable role of superoxide ions, *Applied Catalysis B: Environmental*, 182 (2016) 316-325.

[33] H. Wang, W. Zhang, X. Li, J. Li, W. Cen, Q. Li, F. Dong, Highly enhanced visible light photocatalysis and in situ FT-IR studies on Bi metal@ defective BiOCl hierarchical microspheres, *Applied Catalysis B: Environmental*, 225 (2018) 218-227.

[34] Z. F. Huang, J. Song, X. Wang, L. Pan, K. Li, X. Zhang, L. Wang, J.-J. Zou, Switching charge transfer of $\text{C}_3\text{N}_4/\text{W}_{18}\text{O}_{49}$ from type-II to Z-scheme by interfacial band bending for highly efficient photocatalytic hydrogen evolution, *Nano Energy*, 40 (2017) 308-316.

[35] R. Nyholm, A. Berndtsson, N. Martensson, Core level binding energies for the elements Hf to Bi ($Z=72-83$), *Journal of Physics C: Solid State Physics*, 13 (1980) L1091.

- [36] Y. Gao, Y. Huang, Y. Li, Q. Zhang, J. j. Cao, W. Ho, S.C. Lee, Plasmonic Bi/ZnWO₄ Microspheres with Improved Photocatalytic Activity on NO Removal under Visible Light, *ACS Sustainable Chemistry & Engineering*, 4 (2016) 6912-6920.
- [37] M.L. Brongersma, N.J. Halas, P. Nordlander, Plasmon-induced hot carrier science and technology, *Nat Nano*, 10 (2015) 25-34.
- [38] G. Jiang, X. Li, M. Lan, T. Shen, X. Lv, F. Dong, S. Zhang, Monodisperse bismuth nanoparticles decorated graphitic carbon nitride: Enhanced visible-light-response photocatalytic NO removal and reaction pathway, *Applied Catalysis B: Environmental*, 205 (2017) 532-540.
- [39] S.K. Cushing, J. Li, F. Meng, T.R. Senty, S. Suri, M. Zhi, M. Li, A.D. Bristow, N. Wu, Photocatalytic Activity Enhanced by Plasmonic Resonant Energy Transfer from Metal to Semiconductor, *Journal of the American Chemical Society*, 134 (2012) 15033-15041.
- [40] L. Zhang, W. Wang, S. Sun, J. Xu, M. Shang, J. Ren, Hybrid Bi₂SiO₅ mesoporous microspheres with light response for environment decontamination, *Applied Catalysis B: Environmental*, 100 (2010) 97-101.
- [41] A.B. Murphy, Band-gap determination from diffuse reflectance measurements of semiconductor films, and application to photoelectrochemical water-splitting, *Solar Energy Materials and Solar Cells*, 91 (2007) 1326-1337.
- [42] J.A. Weil, A review of electron spin spectroscopy and its application to the study of paramagnetic defects in crystalline quartz, *Physics and Chemistry of Minerals*, 10 (1984) 149-165.

- [43] K. Wang, Q. Li, B. Liu, B. Cheng, W. Ho, J. Yu, Sulfur-doped g-C₃N₄ with enhanced photocatalytic CO₂-reduction performance, *Applied Catalysis B: Environmental*, 176-177 (2015) 44-52.
- [44] Z.-A. Lan, G. Zhang, X. Wang, A facile synthesis of Br-modified g-C₃N₄ semiconductors for photoredox water splitting, *Applied Catalysis B: Environmental*, 192 (2016) 116-125.
- [45] D. Zheng, C. Pang, Y. Liu, X. Wang, Shell-engineering of hollow g-C₃N₄ nanospheres via copolymerization for photocatalytic hydrogen evolution, *Chemical Communications*, 51 (2015) 9706-9709.
- [46] J.X. Zheng, G. Ceder, T. Maxisch, W.K. Chim, W.K. Choi, First-principles study of native point defects in hafnia and zirconia, *Physical Review B*, 75 (2007) 104112.
- [47] H. Li, J. Shang, Z. Yang, W. Shen, Z. Ai, L. Zhang, Oxygen Vacancy Associated Surface Fenton Chemistry: Surface Structure Dependent Hydroxyl Radicals Generation and Substrate Dependent Reactivity, *Environmental Science & Technology*, 51 (2017) 5685-5694.
- [48] H. Li, J. Li, Z. Ai, F. Jia, L. Zhang, Oxygen Vacancy- Mediated Photocatalysis of BiOCl: Reactivity, Selectivity, and Perspectives, *Angewandte Chemie International Edition*, 57 (2018) 122-138.
- [49] G. Henkelman, A. Arnaldsson, H. Jónsson, A fast and robust algorithm for Bader decomposition of charge density, *Computational Materials Science*, 36 (2006) 354-360.
- [50] G. Giammona, B. Carlisi, S. Palazzo, Reaction of α,β -poly(N-hydroxyethyl)-DL-aspartamide with derivatives of carboxylic acids,

- Journal of Polymer Science Part A: Polymer Chemistry, 25 (1987) 2813-2818.
- [51] K. Hadjiivanov, V. Bushev, M. Kantcheva, D. Klissurski, Infrared-Spectroscopy Study of the Species Arising During NO₂ Adsorption on TiO₂ (Anatase), Langmuir, 10 (1994) 464-471.
- [52] K. Hadjiivanov, V. Avreyska, D. Klissurski, T. Marinova, Surface Species Formed after NO Adsorption and NO + O₂ Coadsorption on ZrO₂ and Sulfated ZrO₂: An FTIR Spectroscopic Study, Langmuir, 18 (2002) 1619-1625.
- [53] K.I. Hadjiivanov, Identification of Neutral and Charged N x O y Surface Species by IR Spectroscopy, Catalysis Reviews, 42 (2000) 71-144.
- [54] L. Sivachandiran, F. Thevenet, A. Rousseau, D. Bianchi, NO₂ adsorption mechanism on TiO₂: An in-situ transmission infrared spectroscopy study, Applied Catalysis B: Environmental, 198 (2016) 411-419.
- [55] R.V. Mikhaylov, A.A. Lisachenko, B.N. Shelimov, V.B. Kazansky, G. Martra, S. Coluccia, FTIR and TPD Study of the Room Temperature Interaction of a NO–Oxygen Mixture and of NO₂ with Titanium Dioxide, Journal of Physical Chemistry C, 117 (2013) 10345-10352.
- [56] P. Chen, F. Dong, Maoxi Ran, Jiarui Li, Synergistic photo-thermal catalytic NO purification on MnOx/g-C₃N₄: enhanced performance and reaction mechanism, Chinese Journal of Catalysis, 39 (2018) 619-629.
- [57] J. Li, Z. Zhang, W. Cui, H. Wang, W. Cen, G. Johnson, G. Jiang, S. Zhang, F. Dong, The Spatially Oriented Charge Flow and Photocatalysis Mechanism on Internal van der Waals Heterostructures Enhanced g-C₃N₄, ACS Catalysis, 8 (2018) 8376-8385.

[58] X. Dong, J. Li, Q. Xing, Y. Zhou, H. Huang, **F. Dong**, The activation of reactants and intermediates promotes the selective photocatalytic NO conversion on electron-localized Sr-intercalated g-C₃N₄, *Applied Catalysis B: Environmental*, 232 (2018) 69-76.

Figure captions

Fig. 1 Projected density of states (PDOS) of Bi atom, BiOSi and Bi@BiOSi (a). The charge difference between each atom in Bi@BiOSi structure (b). Purple, red and blue spheres depict Bi, O and Si atoms. Charge-accumulation and charge-depletion regions are shown in blue and yellow, respectively.

Fig. 2 XRD patterns of BiOSi and Bi@BiOSi samples (a), XPS spectra of Bi4f in BiOSi and Bi@BiOSi-3 (b), SEM images of BiOSi (c) and Bi@BiOSi-3 (d), HRTEM image of Bi@BiOSi-3 (e).

Fig. 3 Visible light photocatalytic performances (a) and the UV-vis diffuse reflectance spectra of BiOSi and Bi@BiOSi samples (b).

Fig. 4 Solid-state EPR spectra of BiOSi and Bi@BiOSi samples (a). DMPO ESR spectra of $\cdot\text{O}_2^-$ in methanolic dispersions in the dark and under visible light irradiation ($\lambda \geq 420$ nm) (b). NO and O₂ coadsorption in BiOSi (c) and side-Bi-BiOSi (d) configuration. All lengths are given in Å, with the color coding of atoms matching that of Fig. 1.

Fig. 5 In situ DRIFT spectra recorded during NO photocatalytic reaction over BiOSi (a) and Bi@BiOSi samples (b-f).

Fig. 6 Normalized the reaction intermediates and final products on each sample after the adsorption stage (a) and photocatalytic reaction stage (b).

Fig. 7 Schematic illustration of the synergistic effects of OVs and Bi metal on the photocatalytic activity.

Fig. 8 Scheme of processes occurring during visible-light-driven photocatalytic NO removal on Bi@BiOSi-3.

Fig. 1

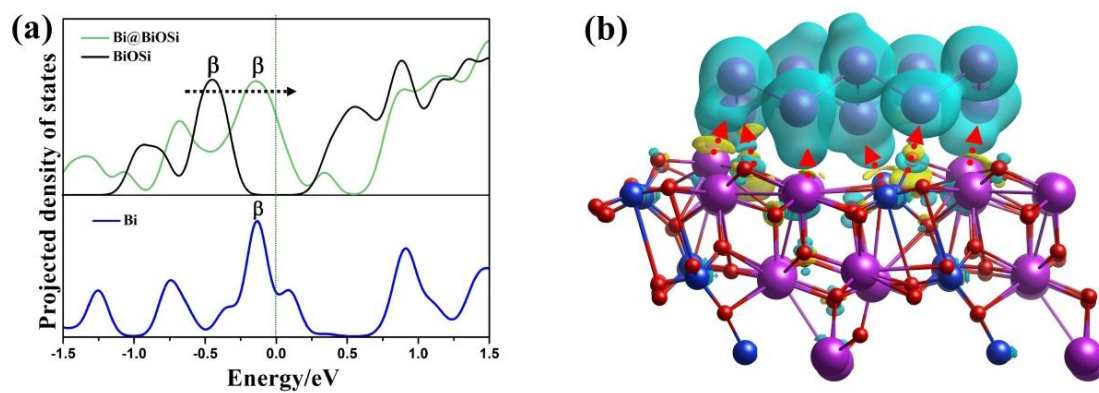


Fig. 2

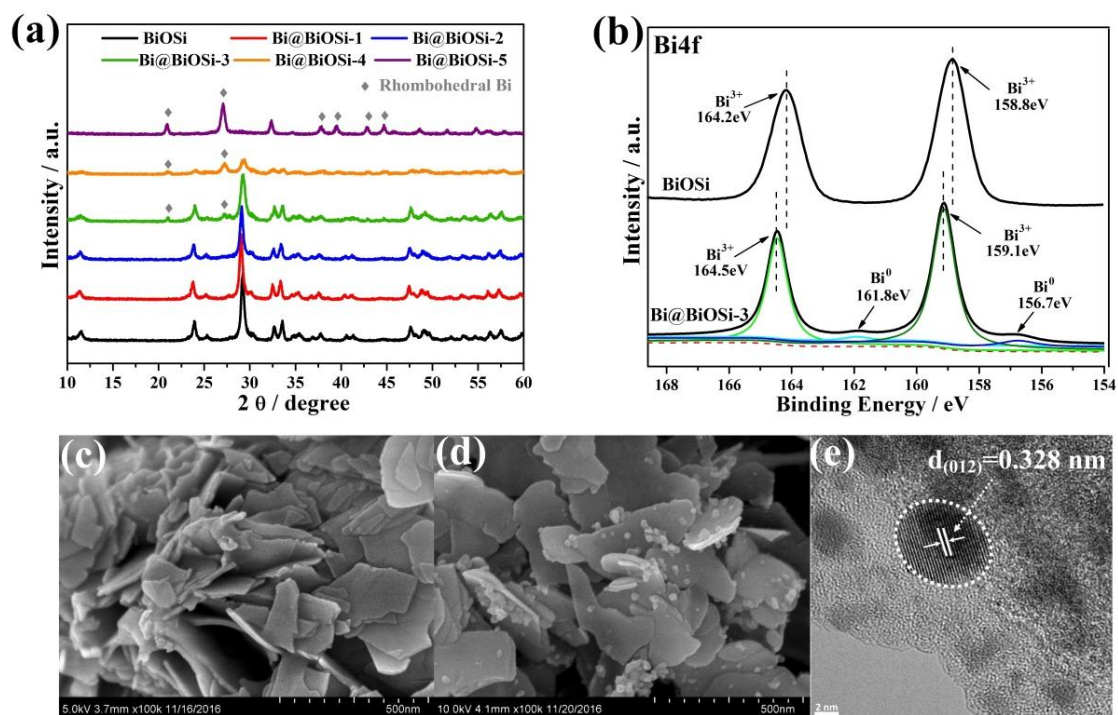


Fig. 3

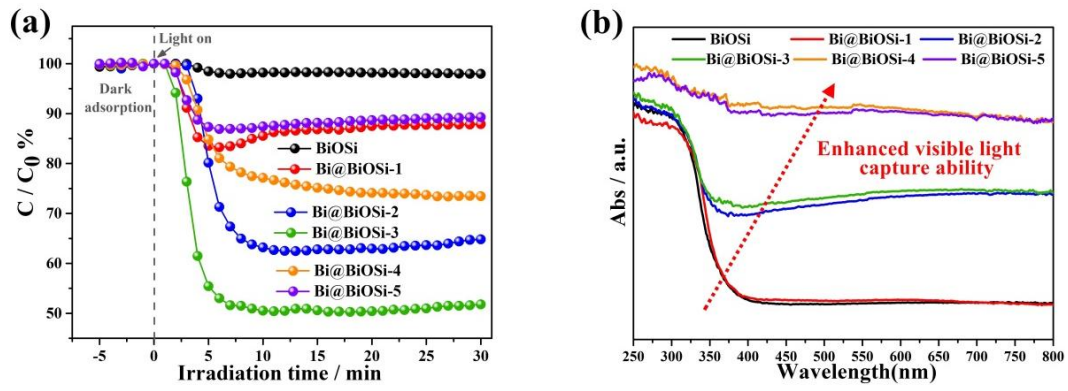


Fig. 4

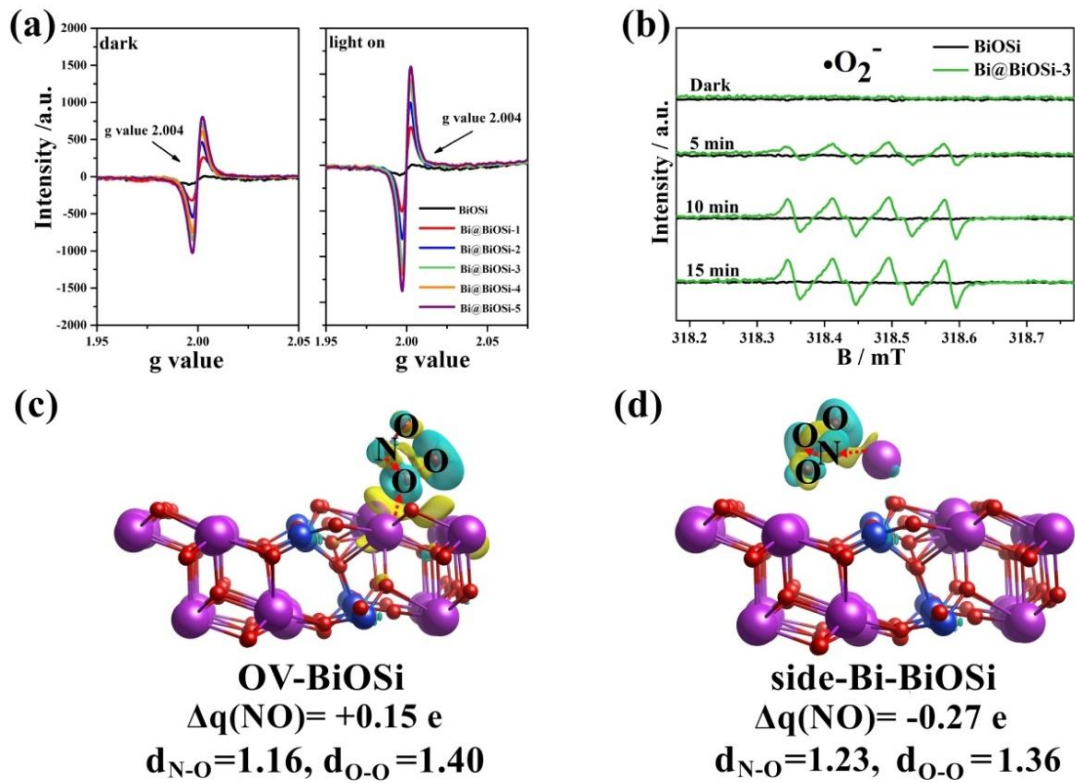


Fig. 5

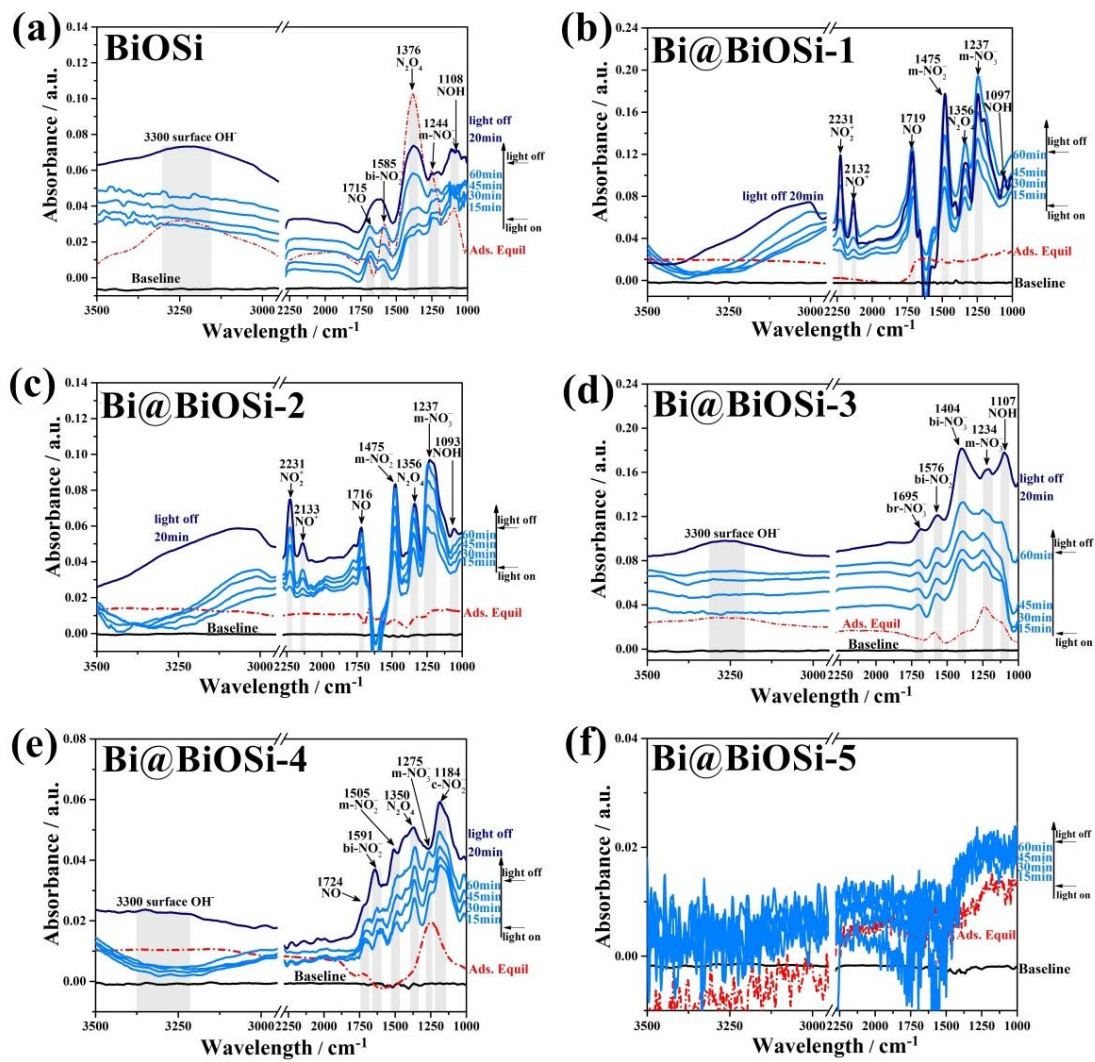


Fig. 6

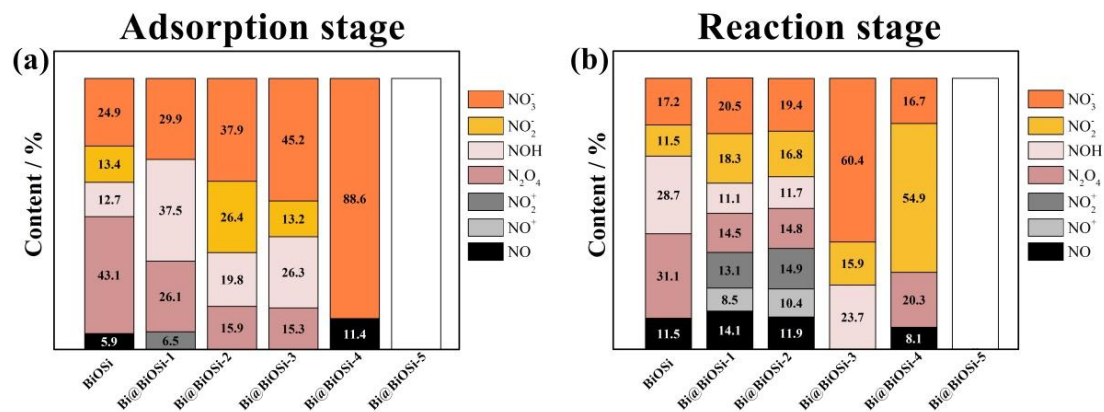


Fig. 7

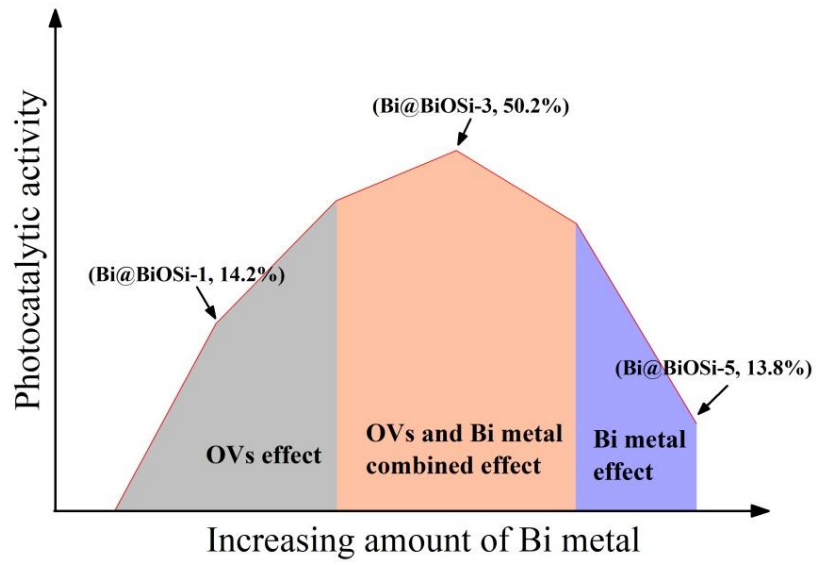
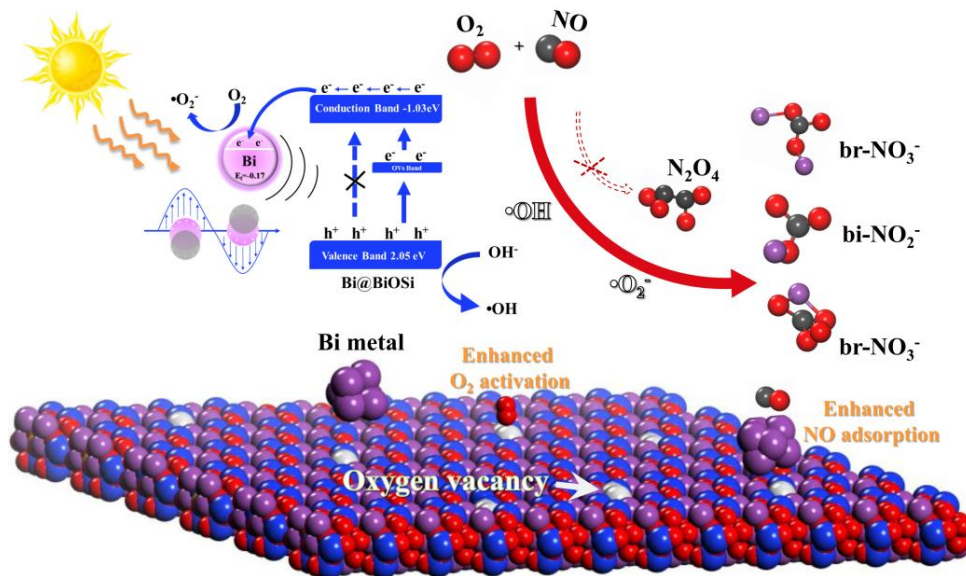
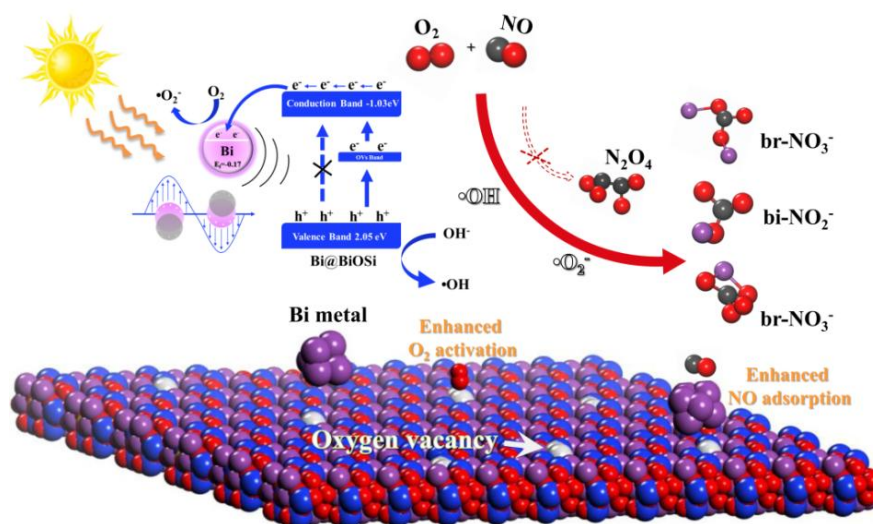


Fig. 8



Graphical abstract

□ Bi@Bi₂O₂SiO₃ catalysts are fabricated for NO photocatalytic removal and the toxic intermediates can be inhibited with the synergistic effects of Bi metal and oxygen vacancy.



Research Highlights

- Bi@Bi₂O₂SiO₃ with oxygen vacancies (OVs) are fabricated by a facile method.
- The surface plasmon resonance of Bi metal enabled charge separation efficiency.
- OVs induced the formation of a mid-gap level in the wide band gap of Bi₂O₂SiO₃.
- The OVs and Bi metal had synergy effects on inhibition of toxic intermediates.
- The photocatalytic reaction mechanism was revealed via in situ DRIFTS.